Repeatability Evaluation Using Contact Finite Element Modeling

Kazunori SHINOHARA[1], Kosei ISHIMURA[2], Yoshiro OGI[3],
Hiroaki TANAKA[4], Koji MATSUMOTO[5]

Summary

High-precision deployable antennas have been developed for artificial satellites. To meet future demand for such antennas, we developed hinge and latch mechanisms with deployment repeatability, based on solid-type mechanical contact connections. The latch mechanism consists of a pair of mechanical structures/parts that come into contact with each other at their respective surfaces. Kinematic couplings are attached to the latch mechanism, which constrain the relative freedom of motion of the two constituent structures. In this study, we compared the experimental repeatability results for the latch structure of the solid-type antenna with computational results based on the contact finite element method (FEM). Developing a robust and efficient contact FEM is one of the most challenging tasks in deployable antenna FEM problems. To facilitate computation of the repeatability of the latch structure, modeling techniques for the contact interactions between two deformable bodies were developed.

Keywords：Satellite, Deployable Structure, Contact, Friction, Finite Element Analysis

1. Introduction

Rockets represent the only way to transport satellites into space at present, and have limited available room to carry a satellite. In this respect, a deployable mechanism is required in order to fold a large antenna. Large deployable antennas are associated, however, with various technical issues, including those associated with: a) precise positioning control, such as the case of the parabolic antenna, and b) instability due to incomplete expansion. A major reason for such technical issues is the friction between parts that are in contact. As satellite observation systems become more sophisticated and highly developed, the demand for large and precise structural parts is increasing. In accordance to the literature, deployable antennas used thus far, are either mesh antennas (e.g., ETS-VIII [1]) or solid antennas (e.g., JWST [2] and LIDAR [3]).

To meet the future demand for high-precision deployable antennas, hinge and latch parts with deployment repeatability were developed, based on the mechanical contact connections. To verify proper functionality of the deployable latch parts in the solid antenna, we used a testbed comprising of contact facing surfaces with several attached fittings. When the two plates are overlaid, a slight shift occurs between them.

The contact state between the two plates depends on the shape or position of the parts on the plate. As time elapses, the contact area and friction vary locally because of the

[1] Department of Integrated Mechanical Engineering, Daido University, Nagoya, Japan
[2] Institute of Space and Astronautical Science (ISAS), JAXA, Sagamihara, Japan
[3] Oxford Space Systems Ltd., Harwell, United Kingdom
[4] Department of Aerospace Engineering, National Defense Academy of Japan, Yokosuka, Japan
[5] Research and Development Directorate, JAXA, Chofu, Japan

deformation and sliding of the parts in contact. The testbed was used (i.e., the latch deployable structure), to study the displacement repeatability, based on the rotational angles between the initial and subsequent positions of a plate after repositioning [4]. In the effort to create a computational model for the testbed, the contact model of this structure becomes an important problem.

To the best of our knowledge, no repeatability calculation results relevant to both the backlash and shift of a latch structure have ever been published. To predict the latch repeatability, a computational model based on the finite element method (FEM) for the contact interactions between the two deformable bodies was developed.

2. Structure of the Solid Antenna

Fig. 1 shows the solid antenna. A folding mechanism is needed to fold the parabolic structure. The mechanism consists of the plates, hinges, and couplings. The plates are fixed to each other through the couplings that is the contact points. Coupling arrangements on the plate and the coupling contact state affect the position accuracy of the parabolic antenna surface.

Fig. 2–Fig. 4 show the conceptual design schematics of the couplings. The couplings are sets of sphere-flat, sphere-vee and sphere-cup fittings that constrain motion to six relative degrees of freedom. As shown in Fig. 2, the sphere-flat consists of a sphere and a plate. The relative displacement between the plate and the sphere is fixed by friction. In this paper, the sphere-flat is referred to as “1DOR” [Degree Of Redundancy (DOR)]. 1DOR has a contact state between a plain surface and the spherical cap, and it constrains motion to one degree of freedom. As shown in Fig. 3, the sphere-vee consists of both the spherical cap and a V-shaped channel, subsequently referred to as “2DOR”. 2DOR has a contact state between a V-shaped channel and the sphere and constrains motion to two degrees of freedom. As shown in Fig. 4, the sphere-cup consists of both the sphere and a conical shape. In a similar manner, the sphere-cup is referred herein to as “3DOR”. 3DOR has a contact state between a conical shape and the sphere and constrains motion to three degrees of freedom. The principle of an object constrained by the kinematic coupling is applied, similar to the cases of machining devices and optical instruments for which positioning accuracy is required.

As shown in Fig. 5, the sphere is sliced so that kinematic couplings can be implemented in the limited space between the upper plate and the lower plate. Similarly, to make the V-groove shown in Fig. 3 shallow, the area around the two contact points between the sphere and the V-groove is extracted from the structure shown in Fig. 3. Therefore, the slice from the spherical shape is constructed as shown in Fig. 6. In the case of Fig. 4 (3DOR), the structure shown in Fig. 7 is constructed by the same means.

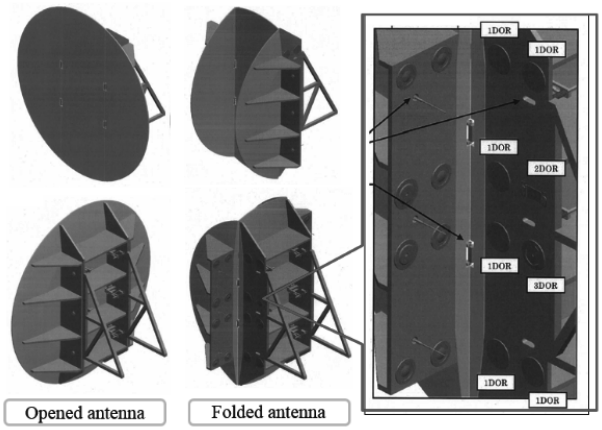

Fig. 1. Structure of solid antenna with contact parts (1DOR, 2DOR, and 3DOR)

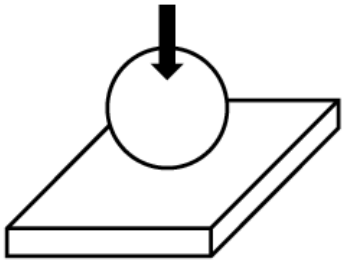

Fig. 2 Sphere-flat (Conceptual figure of 1DOR)

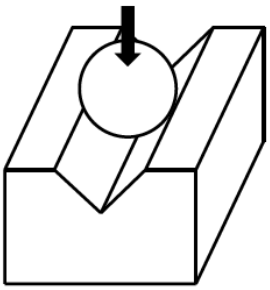

Fig. 3 Sphere-vee (Conceptual figure of 2DOR)

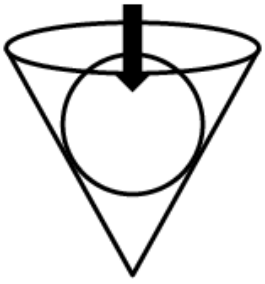

Fig. 4 Sphere-cup (Conceptual figure of 3DOR)

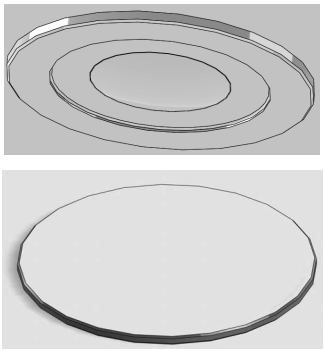

Fig. 5 Implemented 1DOR

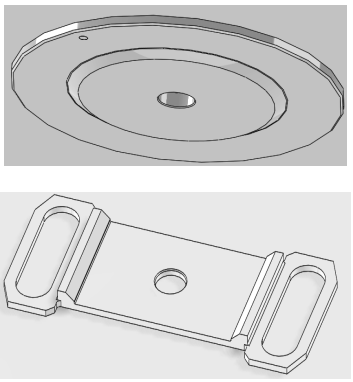

Fig. 6 Implemented 2DOR

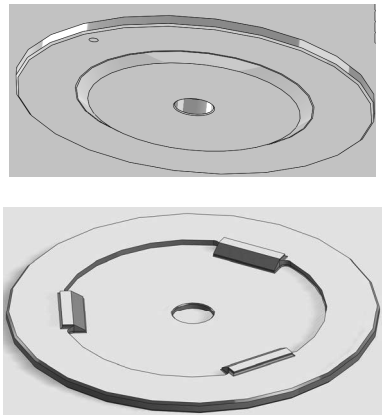

Fig. 7 Implemented 3DOR

3. Test of Latch Deployable Structure

Figs. 8 and 9 show the testbed of the latch deployable structure. The structure consists of two plates: the upper and the lower. The two plates are made from iron and come in contact at three locations on each plate, namely at contact states 1DOR, 2DOR, and 3DOR. 1DOR, 2DOR, and 3DOR are made from SUS440C and include mechanical structures to support each plate at one, two, and three contact points, respectively. The displacement of the lower plate is fixed. Lifting the upper plate draws it away from the lower plate. The upper plate is subsequently lowered toward the lower plate so that the two come in contact with each other. The rotational angles are measured by determining the displacement between the initial and subsequent positions of the upper plate. Table 1 represents the testbed results for the rotation with respect to the x-, y-, and z-axes. The symbol ◎ in the figure 8 represents the positive direction of the z-axis. The positive direction is defined as the outward normal to the plane of the paper.

At small angles, the upper plate becomes parallel with respect to the lower plate. At large angles, there is a slight relative displacement between the initial and subsequent positions of the upper plate. This relative displacement between the plates occurs because of a partial contact state of 1DOR, 2DOR, and 3DOR. In the testbed results, after the upper plate was repositioned on the lower plate, the relative displacements between the upper and lower plates with respect to the x- and y-axes were approximately ±0.1 mm. As shown in Table 1, the absolute values of the rotational angles were measured repeatedly, eight separate times. The average rotational angles along the z-, x-, and y-axes were 4.42, 3.49, and 2.60 arcsec, respectively.

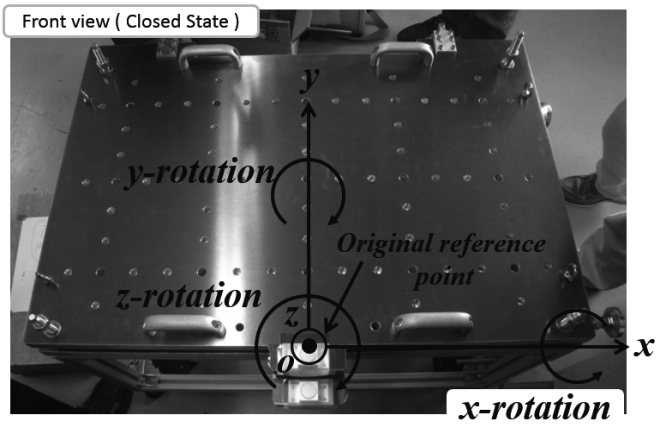

Fig. 8. Testbed [4]

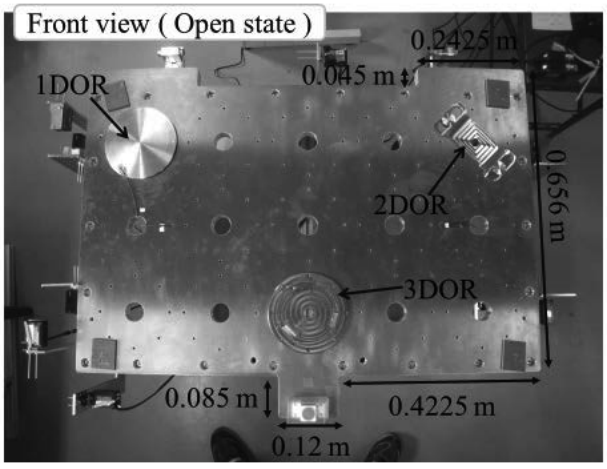

Fig. 9. Configuration of latch structure with contact parts (1DOR, 2DOR, and 3DOR) [4]

Table 1. Rotational angle of upper plate computed as differences between the initial and subsequent positions [4]

	z rotational angle (arcsec)	*x* rotational angle (arcsec)	*y* rotational angle (arcsec)
Testbed data (absolute value)	1.08	2.25	2.58
	0.48	5.09	4.68
	6.73	1.19	0.93
	10.11	1.81	5.00
	5.18	5.52	2.43
	6.54	2.00	3.82
	2.99	5.44	0.59
	2.24	4.53	0.74
Average value	4.42	3.49	2.60

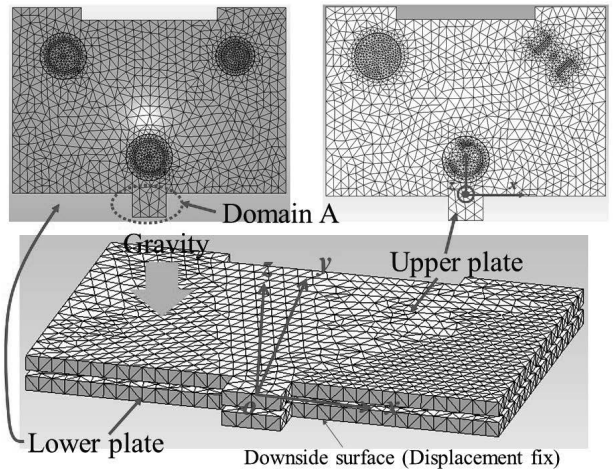

Fig. 10. Computational model

4. Computational Model

To explain the mechanism of the partial contact state on contact parts, we also attempted to construct an FEM computational model based on the latch deployable antenna. Fig. 10 shows the computational model and Table 2 lists the material properties used in the model. Indicatively, the Young's modulus, density, coefficient of friction, and Poisson ratio values were set to 210 GPa, 7874 kg/m^3, 0.17, and 0.3, respectively. The displacement of the downside surface (Fig. 10) on the lower plate is fixed. The model had approximate 48,000 nodes and 27,000 tetrahedral elements. In order to calculate the contact state with high accuracy, the FEM model divided the contact parts into small segments relative to the actual plate segments. The model was loaded with the force of gravity with respect to the negative z-axis. In the testbed, the relative displacements between the lower and upper plates were measured to be ±0.1 mm with respect to the x- and y-axes. Therefore, the relative displacements in the computational model were also set to ±0.1 mm with respect to the x- and y-axes. Figs. 11–19 show the nine calculation conditions of the relative displacements between the upper and lower plates with values (x, y) = (0.0, 0.0), (0.1, 0.0), (0.1, -0.1), (0.0, -0.1), (-0.1, -0.1), (-0.1, 0.0), (-0.1, 0.1), (0.0, 0.1) and (0.1, 0.1). These were defined as conditions 1–9, respectively.

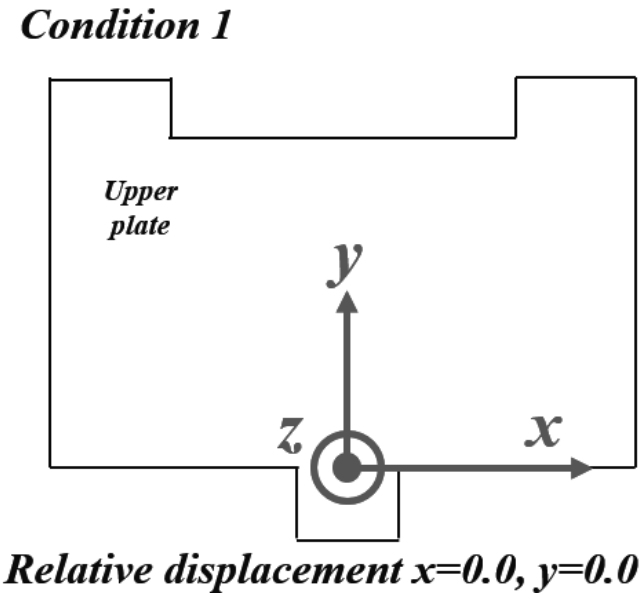

Fig. 11. Condition 1 of computational model

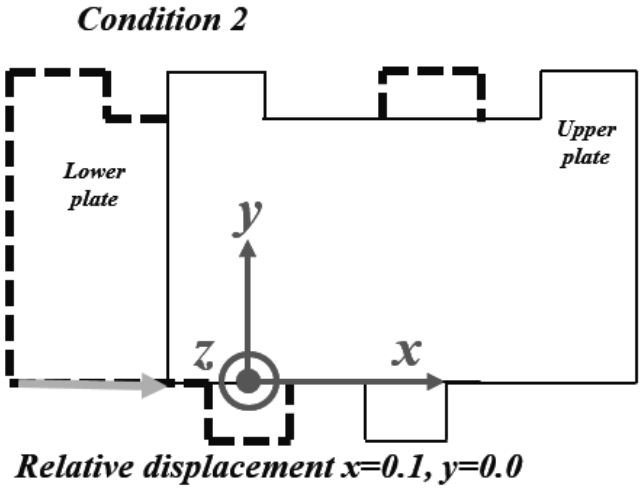

Fig. 12. Condition 2 of computational model

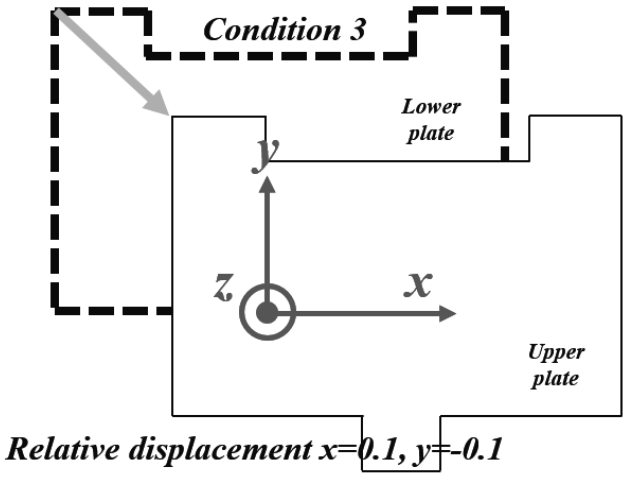

Fig. 13. Condition 3 of computational model

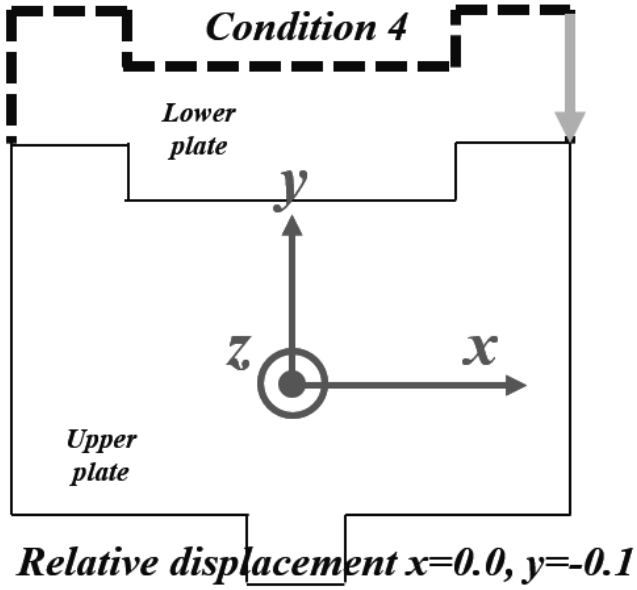

Fig. 14. Condition 4 of computational model

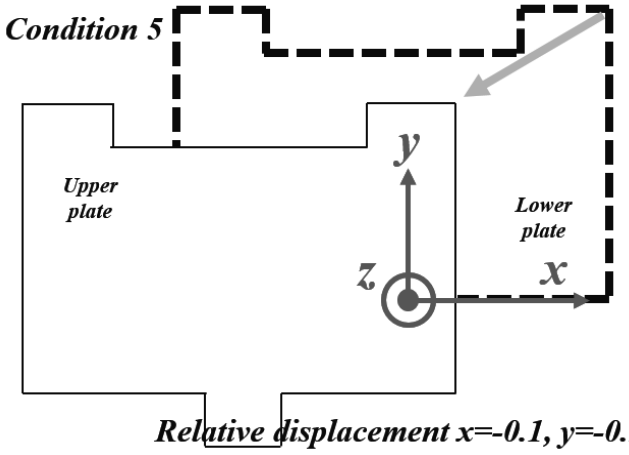

Fig. 15. Condition 5 of computational model

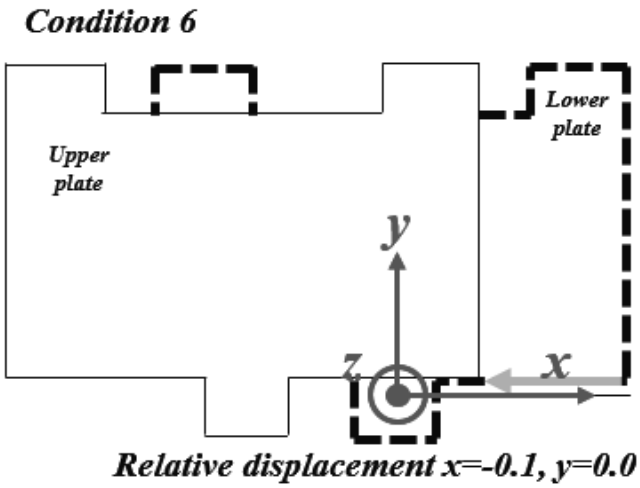

Fig. 16. Condition 6 of computational model

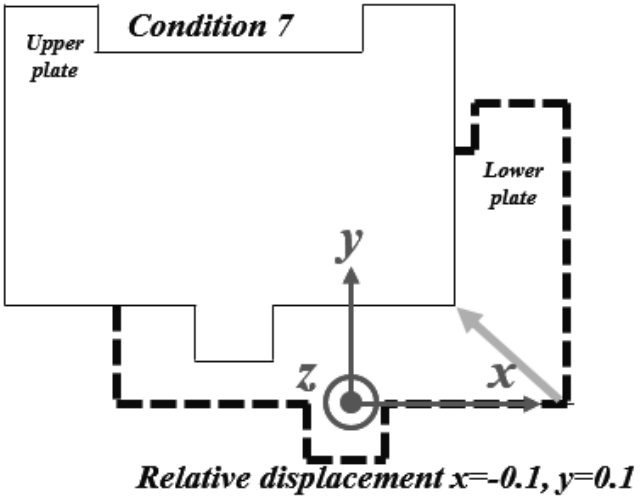

Fig. 17. Condition 7 of computational model

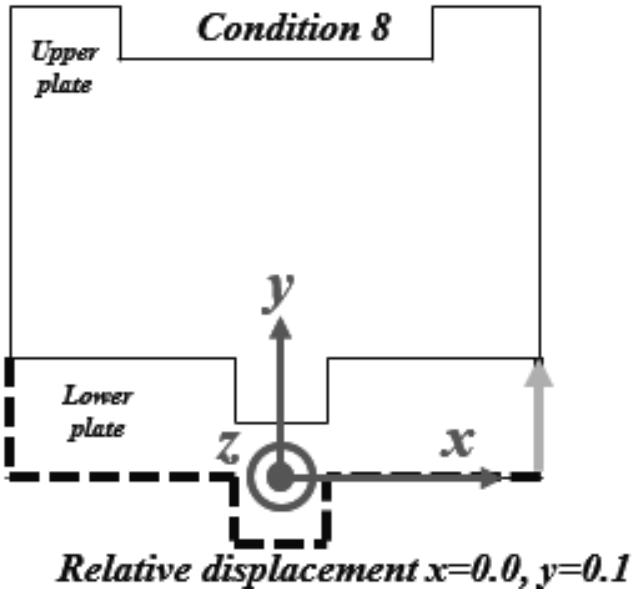

Fig. 18. Condition 8 of computational model

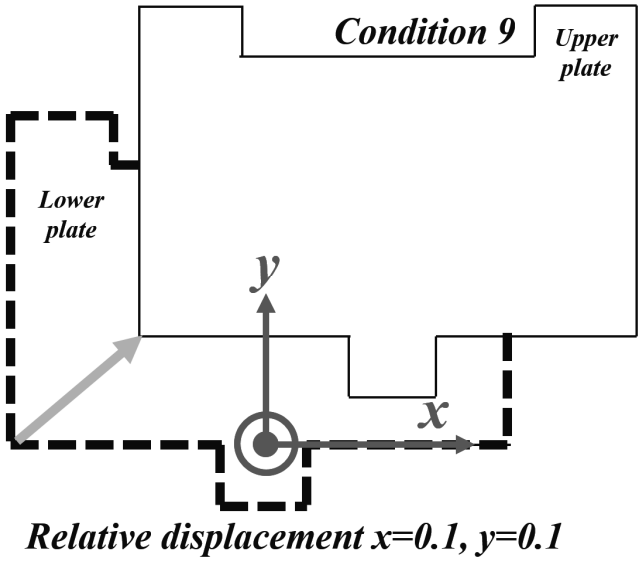

Fig. 19. Condition 9 of computational model

Table 2. Properties of the constructed computational model.

Property	Value
Young's modulus	210 GPa
Density	7874 kg/m^3
Poisson ratio	0.3
Gravity	9.8 m/s^2
Coefficient of friction	0.17
Mass of upper plate	149.5 kg
Mass of lower plate	148.5 kg
Plate thickness	30.0 mm

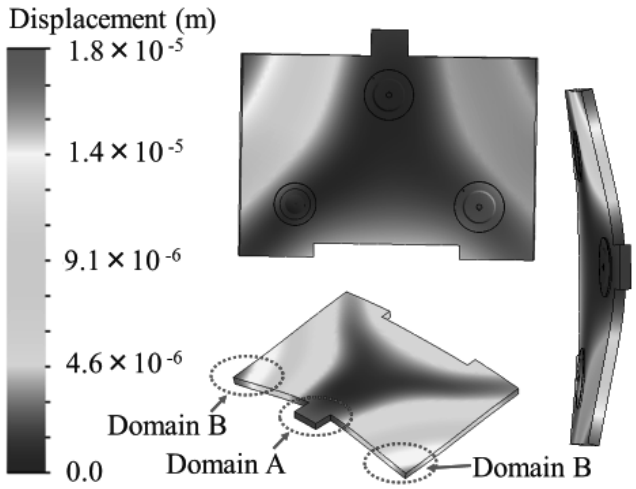

Fig. 20. Displacement contour of the upper plate (condition 1)

5. Computational Results

5.1 Results of complete contact state (condition 1)

The computational model was initially set to condition 1 (see Fig. 11). The x- and y-coordinates of the four edges on the upper plate agreed with those on the lower plate. Fig. 20 shows the resulting displacement contour results. The displacement scale factor of the upper plate was set to 5000. Around the domain A shown in Fig. 20, the upper plate is supported by 3DOR. On the other hand, around the domain B, the upper plate sagged under its own weight.

Figs. 21–27 show the von Mises stress contours. In order to support the self-weight, a stress occurred at 1DOR, 2DOR, and 3DOR. Specifically, Fig. 22 and Fig. 23 show the von Mises stress contour of 1DOR on the upper and lower plates, respectively. The contact state occurred at the center of the sphere in 1DOR. Correspondingly, Fig. 24–27 show the von Mises stress contours of 2DOR and 3DOR on both plates. In such cases, the contact state occurred at two and three points, respectively.

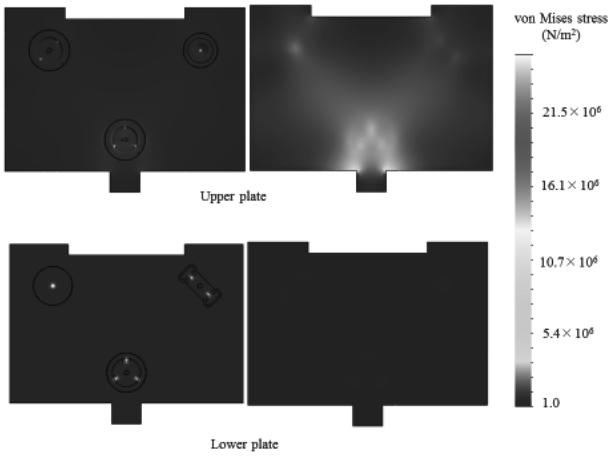

Fig. 21. von Mises stress contour

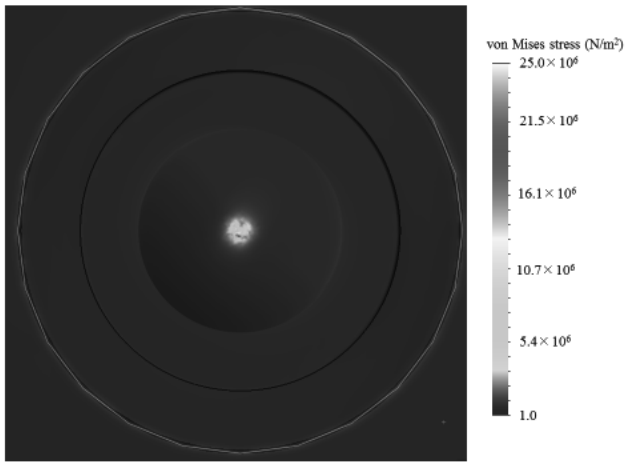

Fig. 22. von Mises stress contour of 1DOR on upper plate

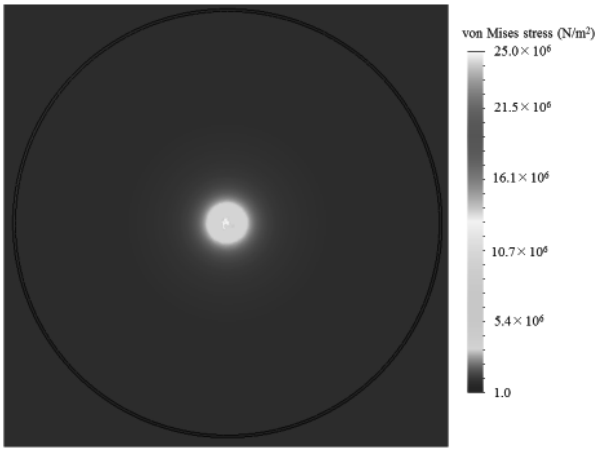

Fig. 23. von Mises stress contour of 1DOR on lower plate

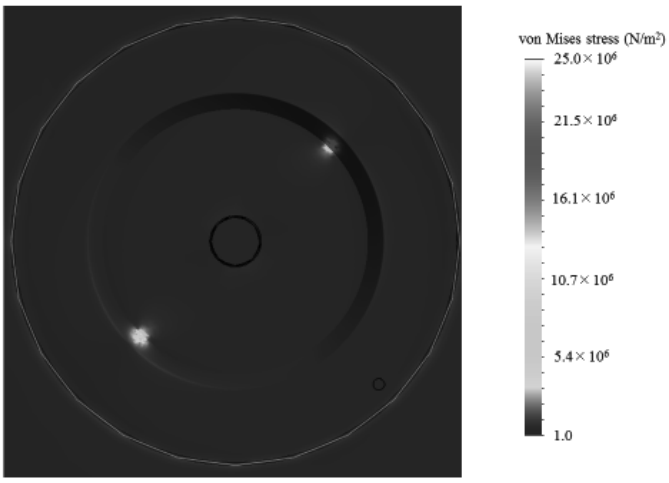

Fig. 24. von Mises stress contour of 2DOR on upper plate

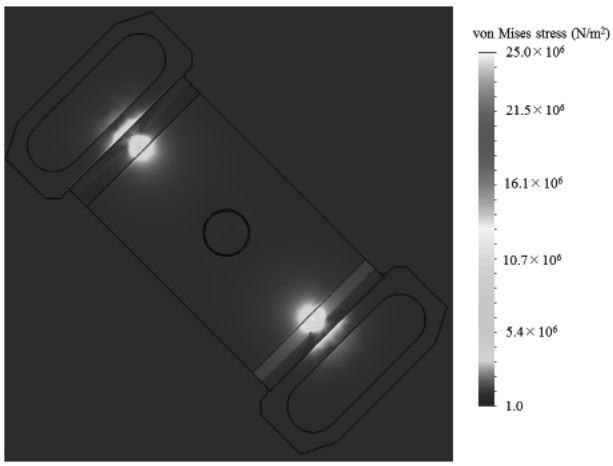

Fig. 25. von Mises stress contour of 2DOR on lower plate.

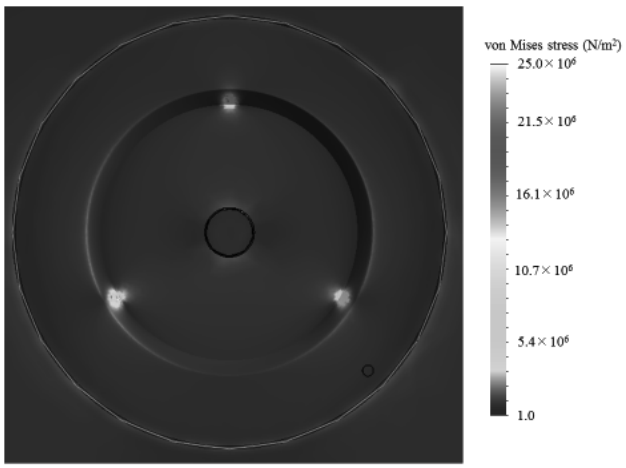

Fig. 26. von Mises stress contour of 3DOR on upper plate

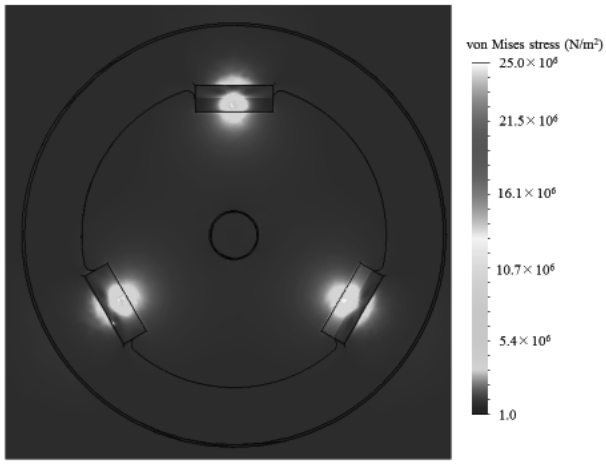

Fig. 27. von Mises stress contour of 3DOR on lower plate

5.2 Results of partial contact state (condition 2)

The case with a given displacement between the upper and lower plates was also calculated. As shown in Fig. 12 (condition 2), the given displacement was set to 0.1 mm with respect to the x-axis.

Fig. 28 shows the displacement contour. The deformation scale factor was set to 5000. As shown in Fig. 20, the contour of the displacement became symmetrical about the left-right axis in the complete contact state. As shown in Fig. 28, the contour of the displacement becomes asymmetrical about the left-right axis under the partial contact state.

Fig. 29–35 show the von Mises stress contour. The partial contact state between the upper and lower plates caused the non-uniform stress distribution at 1DOR, 2DOR, and 3DOR. Additionally, Fig. 30 and Fig. 31 show the von Mises stress contour of 1DOR on the upper and lower plates, respectively, whereas Fig. 32 and Fig. 33 show the corresponding von Mises stress contour of 2DOR. In the partial contact state, the individual weight of the upper plate was supported by

2DOR. Fig. 34 and Fig. 35 show the von Mises stress contour of 3DOR on the upper and lower plates, respectively. In the partial contact state, the individual weight of the upper plate was supported by 3DOR.

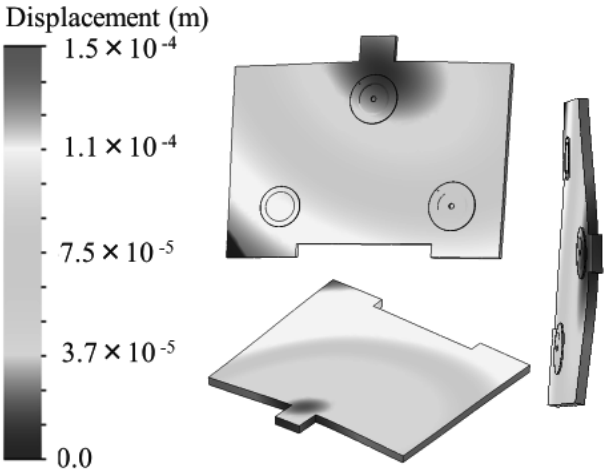

Fig. 28. Displacement contour of upper plate

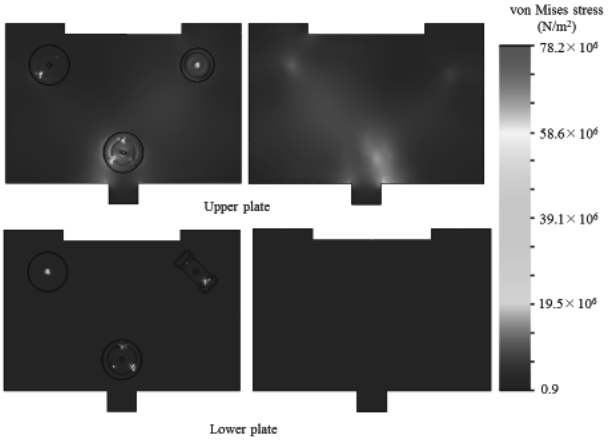

Fig. 29. von Mises stress contour

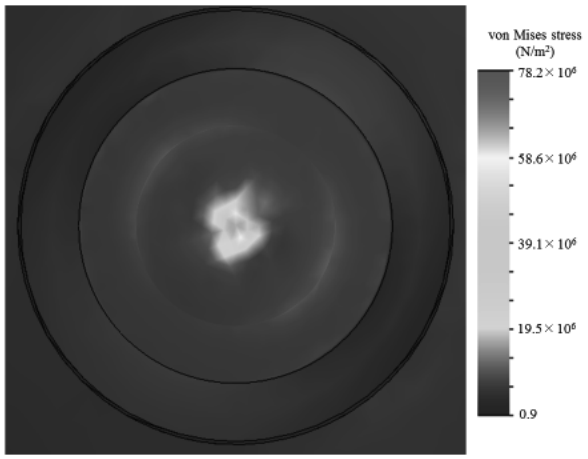

Fig. 30. von Mises stress contour of 1DOR on upper plate

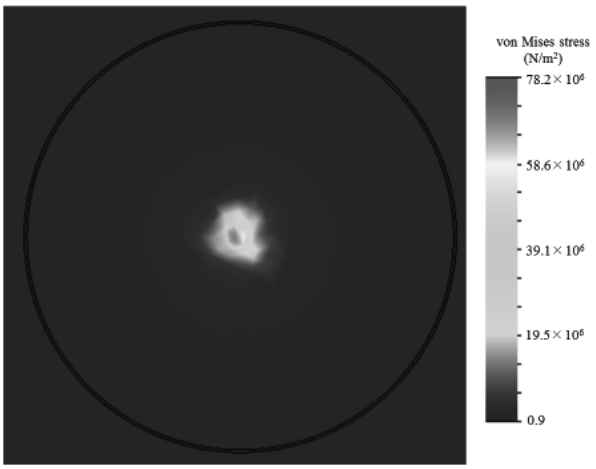

Fig. 31. von Mises stress contour of 1DOR on lower plate

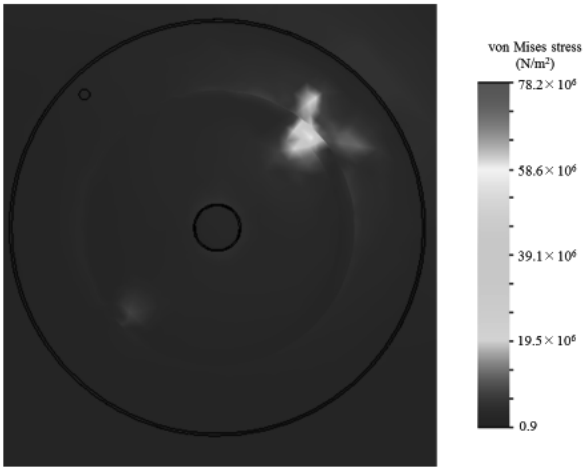

Fig. 32. von Mises stress contour of 2DOR on upper plate

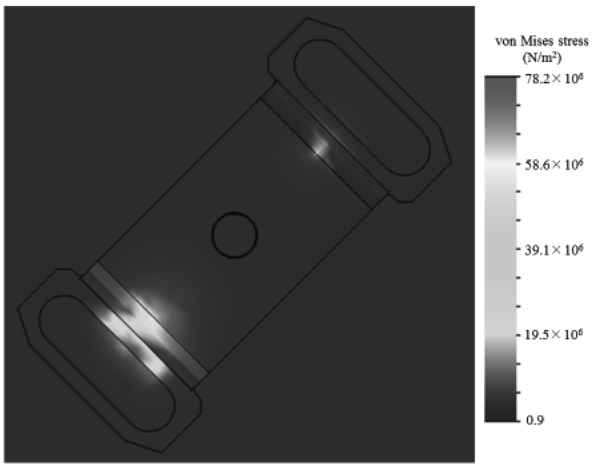

Fig. 33. von Mises stress contour of 2DOR on lower plate

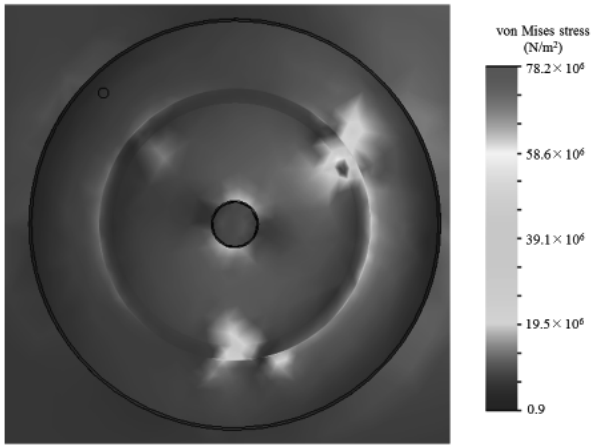

Fig. 34. von Mises stress contour of 3DOR on upper plate

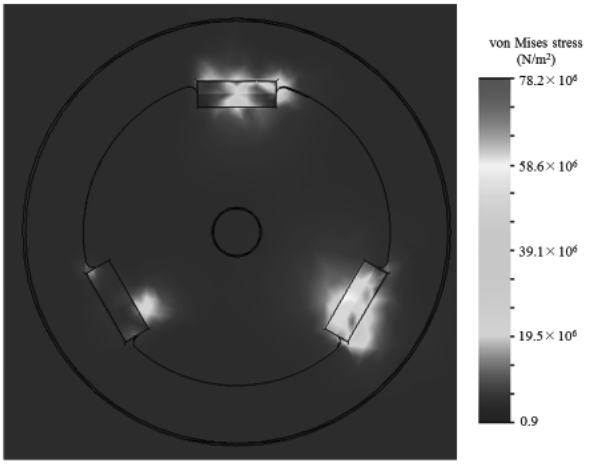

Fig. 35. von Mises stress contour of 3DOR on lower plate

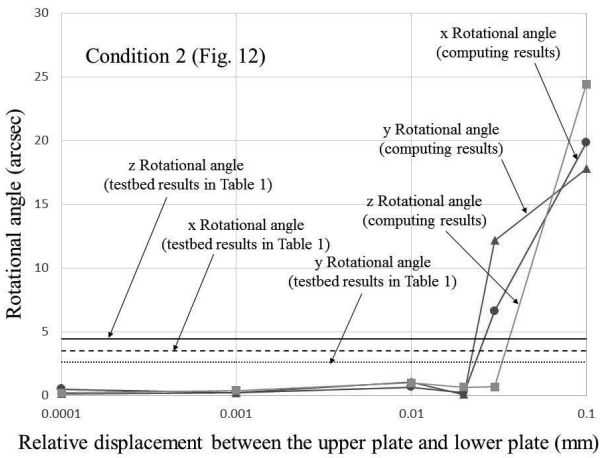

Fig. 36. Semi-log plot of the rotational angles of the upper plate along the direction as shown in Fig. 12

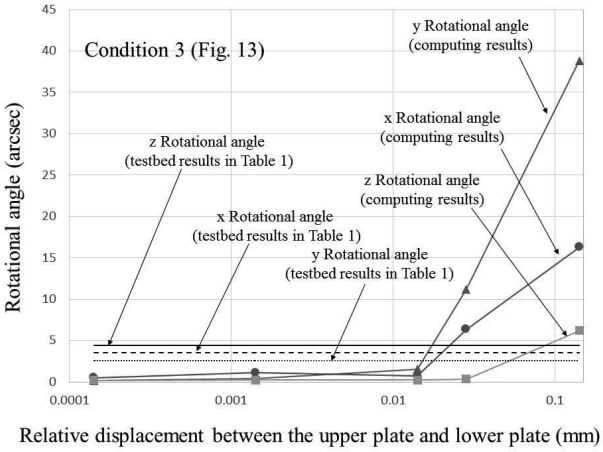

Fig. 37. Semi-log plot of the rotational angles of the upper plate along the direction shown in Fig. 13

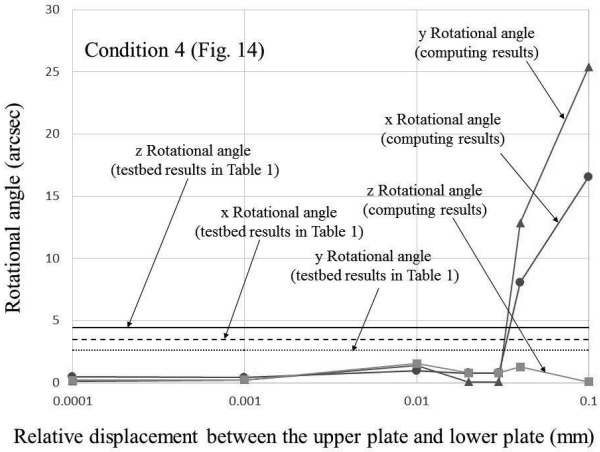

Fig. 38. Semi-log plot of the rotational angles of the upper plate along the direction as shown in Fig. 14

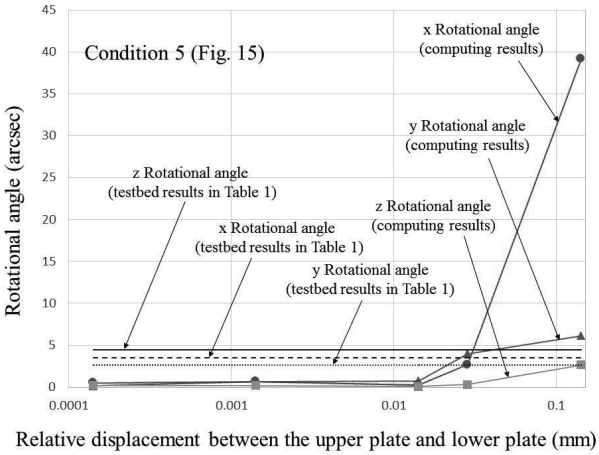

Fig. 39. Semi-log plot of the rotational angles of the upper plate along the direction as shown in Fig. 15

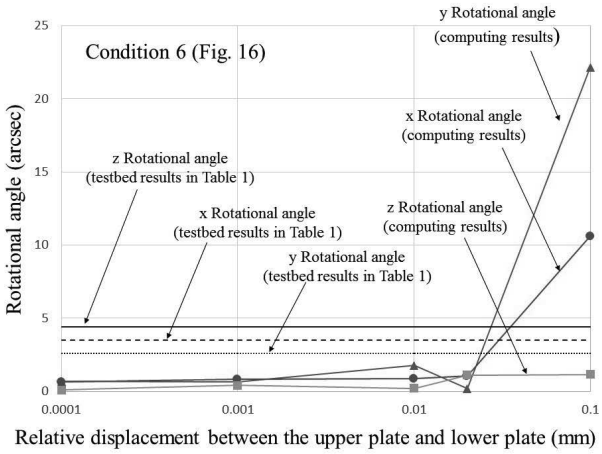

Fig. 40. Semi-log plot of the rotational angles of the upper plate along the direction as shown in Fig. 16

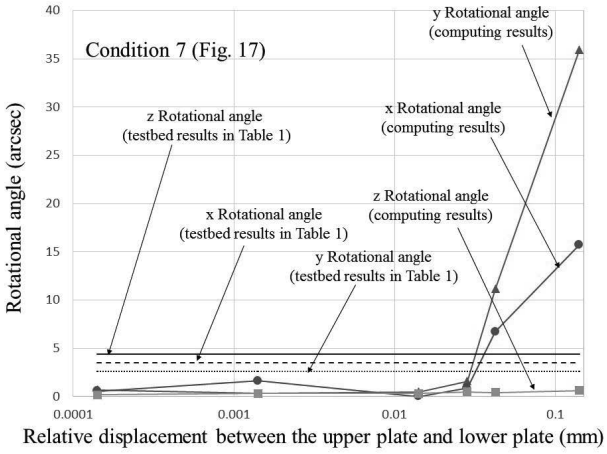

Fig. 41. Semi-log plot of the rotational angles of the upper plate along the direction as shown in Fig. 17

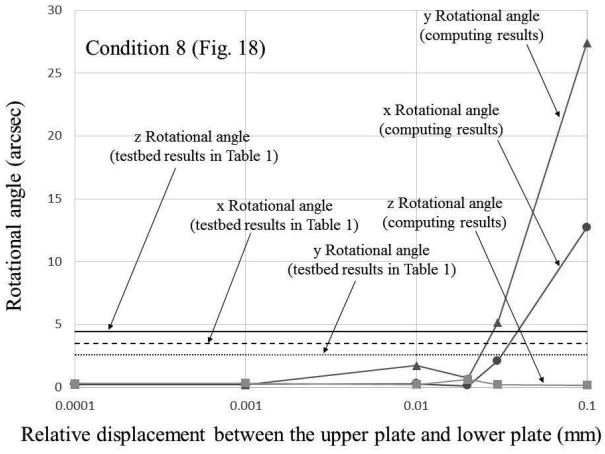

Fig. 42. Semi-log plot of the rotational angles of the upper plate along the direction as shown in Fig. 18

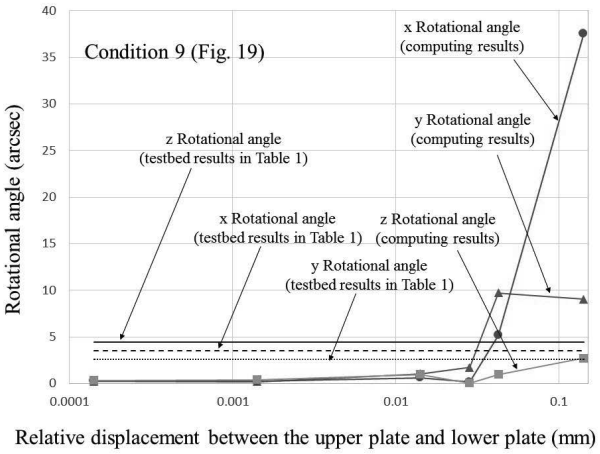

Fig. 43. Semi-log plot of the rotational angles of the upper plate along the direction as shown in Fig. 19

5.3 Comparison of computational and experimental results

Rotational angle data listed in Table 1 was obtained using the measurement equipment. The measurement equipment was placed at the original point in Fig. 8. Therefore, in the computational model shown in Fig. 10, the rotational angles were calculated by using the inclination of the convexity of domain A of the upper plate.

The rotational angles with respect to the relative displacement between the upper and the lower plates are shown in Fig. 36–43. The unit of the rotational angle is arcsec. In Fig. 36-43, Fig. 11–19 represent the direction of the relative displacement. The solid, the dotted thin, and the dotted bold lines in Fig. 36‑43 represent rotational angles in Table 1. The filled □, ○ and △ symbols represent rotational angles with respect to the z-, x- and y-axes, respectively. Compared to the complete contact state, in the partial contact state case, contact points tend to be fewer. Therefore, differences in the rotational angles (which represent the relative displacement between the plates) occurred in the case of partial contact states.

For the testbed, the relative displacement between the upper and lower plates is described in the form of three rotational angles, as presented in Table 1. The three rotational angles decreased within the range of approximately 0.0–10.0. Similarly, as described in Fig. 36–43, with the exception of relative displacements of the order of 0.1 mm, these angles decreased within exactly the same range (approximately 0.0–10.0) in the case of contact state modeling. Therefore, the order of the rotational angles shown in Fig. 36–43 is almost in agreement with those listed in Table 1.

Based on the results of Fig. 36–43, the rotational angles are within a margin of approximately 1.0 arcsec with respect to every direction (Fig. 12–19), given that the relative displacement between the upper and the lower plates is within 0.01 mm. On the other hand, the rotational angle tends to increase irregularly, if the relative displacement becomes larger than 0.01 mm. Therefore, even if the upper and lower plates do not fit perfectly, the repeatability can be achieved when the relative displacements are within the 0.01 mm.

6. Conclusions

For the development of a latch deployable antenna structure with high precision, a technique to evaluate the displacement between two plates based on FEM was presented. The computational and experimental results were compared that lead to the following conclusions.

The rotational angle of the upper plate was measured as the difference between the initial and subsequent positions. A computational model based on FEM was created to obtain the calculated rotational angles between the initial and subsequent positions. The computational results agreed well with the test results.

Through the computational model, information on the repeatability or the backlash mechanism can be obtained, using contact FEM. To quantitatively evaluate the repeatability of the latch structure, information related to repeatability is summarized in the form of rotational angles. Therefore, from an engineering viewpoint, important data can be obtained with sufficient accuracy.

In future research, we will examine optimal arrangements of the contact parts on the plate to minimize changes to the rotational angles.

References

[1] Nakamura, K., Tsutsumi, Y., Tsujihata, A. and Meguro, A.: Large deployable reflector on ETS-VIII, *17th AIAA ICSS Conference,* AIAA-98-1229 (1998).

[2] Reynolds, P., Atkinson, C. and Gliman, L.: Design and Development of the Primary and Secondary Mirror Deployment Systems for the Cryogenic JWST, *37th Aerosp. Mech. Symp.* (2004).

[3] Heald, J. C. and Peterson, L. D.: Deployment Repeatability of a Space Telescope Reflector Petal, *J. Spacecraft and Rockets*, **39** (2002), pp. 771-779.

[4] Ogi, Y., Ishimura, K., Shinohara, K., Matsumoto, K., Tanaka, H., Ito, T. and Kai, K.: Study of High-Precision Deployable Latch Mechanism Using Kinematic Coupling, *28th Symp. Aerosp. Struct. and Mater.* (2013) in Japanese.